

# Lightweight and Fast Real-time Image Enhancement via Decomposition of the Spatial-aware Lookup Tables

Wontae Kim<sup>1,3</sup>, Keuntek Lee<sup>2</sup>, and Nam Ik Cho<sup>1,2</sup>

<sup>1</sup>IPAI, Seoul National University, Seoul, Korea

<sup>2</sup>Department of ECE, INMC, Seoul National University, Seoul, Korea

<sup>3</sup>LG Electronics, Seoul, Korea

{munte2, leekt000, nicho}@snu.ac.kr

## Abstract

The image enhancement methods based on 3D lookup tables (3D LUTs) efficiently reduce both model size and runtime by interpolating pre-calculated values at the vertices. However, the 3D LUT methods have a limitation due to their lack of spatial information, as they convert color values on a point-by-point basis. Although spatial-aware 3D LUT methods address this limitation, they introduce additional modules that require a substantial number of parameters, leading to increased runtime as image resolution increases. To address this issue, we propose a method for generating image-adaptive LUTs by focusing on the redundant parts of the tables. Our efficient framework decomposes a 3D LUT into a linear sum of low-dimensional LUTs and employs singular value decomposition (SVD). Furthermore, we enhance the modules for spatial feature fusion to be more cache-efficient. Extensive experimental results demonstrate that our model effectively decreases both the number of parameters and runtime while maintaining spatial awareness and performance. The code is available at <https://github.com/WontaeaeKim/SVDLUT>.

## 1. Introduction

Automatic photo enhancement has gained attention because it improves the aesthetic quality of images and minimizes the need for manual retouching. Deep learning-based enhancement methods [1, 2, 4, 5, 8, 9, 11, 16–18, 20, 21, 25, 31, 33, 40, 42, 49] have shown impressive results. Especially, 3D LUT methods [22, 28, 29, 38, 43–47] demonstrate an excellent balance between performance, model size, and inference time, even in tasks other than image enhancement [19, 26, 27, 30, 32]. These methods enable the direct retrieval of output values through inter-

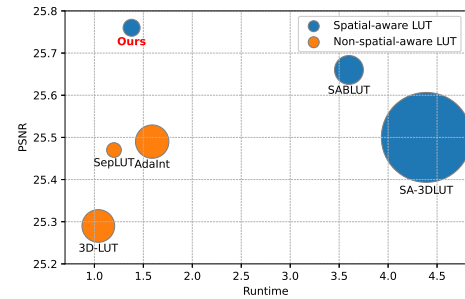


Figure 1. Trade-off between performance and runtime on FiveK dataset [3]. The circle size is proportional to the model size.

polation, eliminating the need for repeated, complex computations. This capability effectively replaces a non-linear color transformation, resulting in reduced computational costs and faster inference times.

Notably, the image-adaptive 3D LUT method [46] outperforms fixed 3D LUT methods by generating a customized 3D LUT for each individual image. However, this method has a limitation in that it does not utilize spatial information. To address this limitation, Wang *et al.* investigated a spatial-aware 3D LUT method [38] that generates and fuses spatial features before applying the 3D LUT for image enhancement. However, the additional processes required for spatial awareness lead to an increase in the number of parameters and inference time, representing a trade-off. More recently, Kim *et al.* [22] have effectively reduced model size; however, the method still suffers from long inference times when processing high-resolution images. To address the limitation of spatial-aware LUT methods, we present a framework that features a compact model size and short inference time while maintaining competitive performance, as illustrated in Fig. 1. To enhance efficiency, we

analyze previous LUT-based image enhancement methods and identify two key insights. First, the 3D LUTs generated for each image can often be redundant and can be effectively replaced with linear operations involving 2D LUTs. Moreover, inspired by singular value decomposition (SVD), the 2D LUT can be substituted with a diagonal matrix and two sparse matrices, resulting in an 88% reduction in the number of parameters compared to the 3D LUT. Second, we observe that previous methods are not cache-efficient when incorporating spatial information, which significantly contributes to long inference times, especially for high-resolution images. Therefore, we propose a cache-efficient spatial information fusion structure that delivers quick inference, even for high-resolution images.

The contributions of this paper are three-fold:

- We introduce a new approach that replaces a 3D LUT with 2D LUTs, which are further simplified by SVD.
- We propose an efficient architecture for the LUT-based image enhancement method that achieves spatial awareness while maintaining a compact model size and short inference time.
- We conduct extensive experiments to evaluate our approach against existing methods using two benchmark datasets. The results demonstrate the efficiency and effectiveness of our method in image enhancement.

## 2. Related Work

### 2.1. Image Enhancement Methods with 3D LUT

Image enhancement methods based on 3D LUTs have gained attention due to their efficient operation and real-time performance [22, 28, 29, 38, 43, 44, 46, 47]. An LUT-based method incorporating deep learning has also been introduced, which predicts weights by a simple CNN and generates image-adaptive 3D LUTs through a weighted sum of basis 3D LUTs [46]. Yang *et al.* enhanced the capacity of LUTs by combining 1D LUTs [44] or adaptive vertices [43] with 3D LUTs. While these advanced LUT methods significantly improve performance, they still face limitations due to a lack of spatial information.

To overcome the limitation, Wang *et al.* proposed the spatial-aware 3D LUT method (SA-3DLUT) [38], which generates spatial features using a U-Net [35] style backbone and combines these features with the input image. Although the spatial awareness tools enhance performance, they require a significant number of parameters and result in longer inference times. Meanwhile, Kim *et al.* replaced the U-Net style decoder with bilateral grids and a slicing operation [22]. This approach effectively reduces the number of parameters; however, the inference time for high-resolution images remains longer than that of other non-spatial-aware methods. Given this trade-off, we investigate the increase in model size and inference time associated with spatial aware-

ness. Based on these insights, we optimize the process of generating spatial awareness using a linear operation of 2D LUT combined with a cache-efficient structure.

### 2.2. LUT Size Reduction

The parameters of 3D LUT-based models are mainly used to generate the values in the table, and reducing the table size is one of the most effective ways to decrease the model’s overall size. A straightforward method for reducing the size of an LUT is to decrease the number of sampling points; however, this can lead to a decline in performance. Zhang *et al.* [47] demonstrated that the output color shows different correlations within each axis; specifically, a strong correlation exists within the same channel axis, while there is a weaker correlation with the other axes. Building on this finding, they proposed the CLUT [47], which uses varying bin sizes based on correlation and decomposes the LUT into one basis LUT and two transformation matrices. Furthermore, Li *et al.* [27] effectively reduced the size of LUTs in super-resolution tasks by employing the Diagonal First Compression (DFC) framework. They found that most pixel values correspond to the entries along the diagonal of the LUTs. Their approach involved compressing the LUTs by subsampling the non-diagonal values and re-indexing the remaining entries. While previous methods have focused on reducing the size of LUTs by subsampling axes with weak correlations, we propose a new strategy that replaces the 3D LUT with linear operations of 2D LUTs with their SVD.

## 3. Proposed Method

### 3.1. Preliminary: Image-adaptive 3D LUT Methods

Most 3D LUT methods [22, 28, 38, 43, 44, 46] enhance the image quality by the following three steps. First, they extract image context feature  $\rho$  from a resized input image  $\hat{X}$ , which can be expressed as

$$\rho = B(\hat{X}), \quad (1)$$

where  $B(\cdot)$  is a simple backbone network. The backbone network can handle images of arbitrary resolution and maintains a small size by using resized images as input.

Second, preprocessing is performed, where various methods have been proposed to enhance its efficiency, such as spatial feature fusion [22, 38], 1D LUT processing [44], or adaptive vertices [43]. Especially, spatial feature fusion is used to provide spatial information in spatial-aware 3D LUT methods, which combines an input image and spatial-aware maps  $f_s \in \mathbb{R}^{K \times W \times H}$ . Spatial-aware maps can be generated by slicing with bilateral grids [22] or U-net style decoder [38]. This step can be described as

$$\bar{X} = F(X, f_s) \quad (2)$$

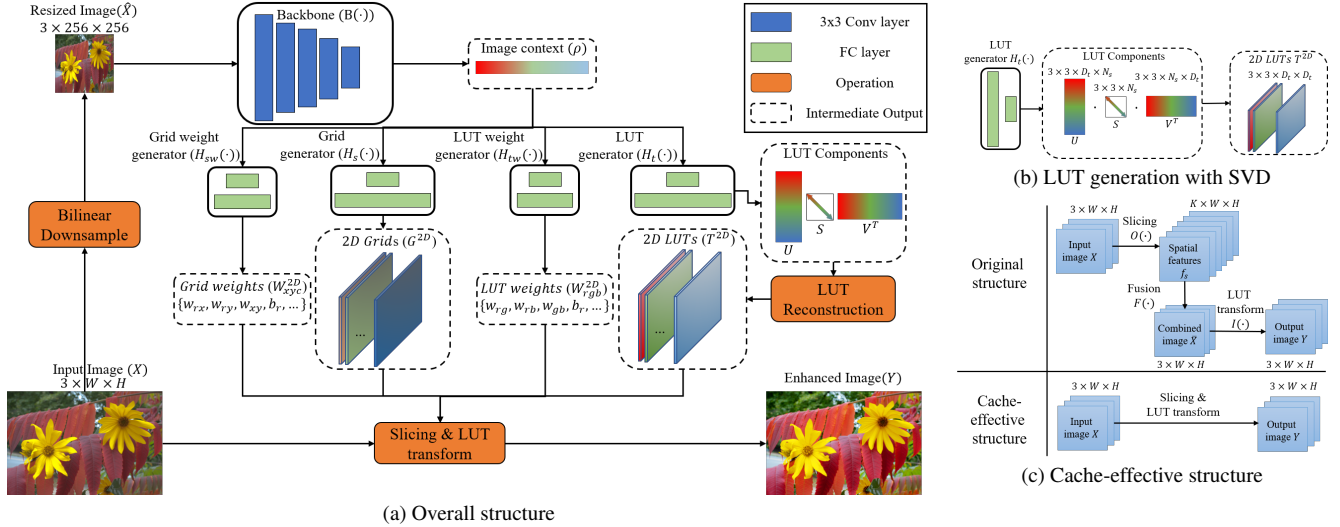


Figure 2. (a) Overall structure of our SVDLUT. The backbone network extracts image context from resized images. The image context is used to predict bilateral grids, LUT components, and weights of LUTs, and bilateral grids. LUTs are reconstructed from LUT components. The input image is enhanced by slicing and LUT transform operation. (b) Process of LUT generation using SVD. (c) Comparison of our cache-effective structure with the original.

where  $F(\cdot)$  is preprocessing operation and  $\bar{X}$  is a preprocessed image.

Finally, they generate image-adaptive 3D LUTs  $T^{3D} \in \{t_{rgb}^c | c \in \{r, g, b\}\}$  from context features  $\rho$ , where  $t_{rgb}^c$  is an LUT which has  $r$ -,  $g$ -, and  $b$ -axis for output channel  $c$ . A 3D LUT  $t_{rgb}^c \in \mathbb{R}^{D_t \times D_t \times D_t}$  is composed of sparsely sampled enhanced color values with  $D_t$  vertices on each axis. Each 3D LUT is used to retrieve the enhanced color values by interpolation.

$$Y_{(c,x,y)} = I_{tri}(\bar{X}_{(c,x,y)}, t_{rgb}^c), \quad T^{3D} = H_t(\rho), \quad (3)$$

where  $Y_{(c,x,y)}$  is the output color value at the corresponding coordinate  $(c, x, y)$ , and  $I_{tri}(\cdot)$  is trilinear interpolation.

### 3.2. SVDLUT

The Fig. 2a shows our spatial-aware 3D LUT framework. Our method effectively addresses the inherent limitations of spatial-aware LUT methods by reducing the number of parameters through decomposition methods and minimizing inference time at high resolution with a cache-effective structure. First of all, image context  $\rho$  is extracted by the same backbone network of SABLUT [22] as described in Eq. (1), since this aspect is not our primary contribution. Second, the generators create LUT components, bilateral grids, and their corresponding weights from the image context. In this operation, we analyze the utilization of 3D LUTs and suggest a decomposition method using low-dimensional LUTs in Sec. 3.2.1. Furthermore, the decomposition method by SVD and the corresponding analysis are also provided in Sec. 3.2.2. The bilateral grid with slicing is

Table 1. Ablation study under different dimensions of LUT and bilateral grid. Each cell indicates PSNR (model size) measured for the photo retouch task on the FiveK dataset.

		Bilateral grid		
		3D	2D	1D
LUT	3D	25.68 (1.3M)	25.67 (1.1M)	25.54 (1.0M)
	2D	25.67 (421.5K)	25.68 (205.3K)	25.53 (161.2k)
	1D	25.37 (335.9K)	25.53 (119.8K)	25.22 (75.7K)

selected to provide spatial awareness, as its structural similarity to LUTs enables the use of the same decomposition techniques. Finally, an input image is enhanced by slicing and LUT transform operation. We found that previous spatial feature fusion incurs a long inference time due to poor cache effectiveness. We introduce a cache-effective operation that combines the slicing and LUT transform in Sec. 3.2.3. The details of the network layers and hyperparameters are provided in the supplementary material.

#### 3.2.1. Decomposition into Lower Dimension

For fixed LUT methods, 3D LUTs have been preferred to lower-dimensional LUTs due to their high capacity, which can universally handle multiple images [36, 44]. However, the size of the 3D LUTs significantly contributes to the overall model size and image-adaptive LUT is generated for a given image. In this context, we analyze the utilization of the 3D LUT to identify ways to reduce the model size. We conduct an experiment to measure the utilization rate of the 3D LUT using the FiveK dataset [3]. The rate indicates the proportion of vertices in the 3D LUT that are actually ref-



and bilateral grid because this combination can reduce the model size by 84% without performance degradation.

### 3.2.2. Singular Value Decomposition (SVD)

After we decompose 3D LUTs into 2D LUTs and bilateral grids, we consider using the SVD to reduce the number of parameters. To verify the efficiency of this approach, we conduct the following toy experiments. We decompose the pre-trained 2D LUTs into singular values  $S$  and two matrices  $U, V$ . After reducing the singular values and corresponding rows of two matrices, we reconstruct the 2D LUT. As can be seen in Fig. 4a, we measure the PSNR of the enhanced image by reconstructed 2D LUT. Fig. 4b presents the results of the same experiment that applies SVD to the bilateral grid. While the LUT maintains its performance with up to eight singular values, the bilateral grid experiences a performance drop from the beginning.

Fig. 4c and Fig. 4d illustrate the performance of models trained from scratch. Specifically, the models predicts LUT components ( $S, U, V$ ) and reconstruct 2D LUTs from those components as illustrated in Fig. 2b like

$$T^{2D} = U \cdot S \cdot V^T, \quad S, U, V^T = H_t(\rho), \quad (9)$$

where  $V^T$  is transposed matrix of  $V$ . These results have a similar tendency to toy examples. The reason seems to be that the LUT has a monotonic and simple structure, whereas the bilateral grid incorporates spatial information. The SVD decomposition is effective when singular values are smaller than 16 for LUT and 8 for bilateral grids. Hence, we decide to apply SVD to the LUT but not to the bilateral grid.

### 3.2.3. Cache-Effective Spatial Feature Fusion

In this section, we explore the processes involved in spatial-aware LUTs and enhance the structure to reduce runtime. To conduct our investigation, we measure the runtime of various modules by adding them incrementally and compare our method with the original structure in [22, 38], as shown in Fig. 2c. As illustrated in the left side of Tab. 2, the runtime of the original structure tends to increase at higher resolutions. This increase is attributed to spatial feature fusion, slicing, and LUT transformations. Specifically, these processes read high-resolution input and write high-resolution intermediate outputs ( $f_s$  and  $\bar{X}$ ), which result in frequent data exchanges between fast, high-rank memory and slow, low-rank memory within memory hierarchies. This frequent exchange is the main reason for the increase in runtime at high resolutions. To address this issue, we combine slicing and LUT transformation to reduce the runtime by minimizing the generation of intermediate outputs and reusing previously calculated results, such as indices of LUT. Additionally, we remove the convolution in Eq. (8) since weighted sum for decomposition can not only replace it but also enhance image-adaptiveness. We effectively reduce the runtime, as can be seen in the right side of Tab. 2,

Table 2. Runtime across modules for original and cache-effective structure.

Original structure			Cache-effective structure		
Component	Runtime(ms)		Component	Runtime(ms)	
	480p	4K		480p	4K
Backbone	0.72	0.73	Backbone	0.72	0.72
Grid/weight Gen	0.23	0.23	Grid/weight Gen	0.23	0.23
Slicing	0.19	0.54	LUT/weight Gen	0.3	0.31
Fusion	0.05	1.6	Slicing & LUT Transform	0.12	0.13
LUT/weight Gen	0.29	0.05			
LUT Transform	0.09	0.7			
Total	1.57	3.84	Total	1.37	1.38

and improve the PSNR by 0.08 dB for the photo retouch task on the FiveK dataset. The cache-effective spatial-aware LUT transform can be described as

$$Y_{(c,x,y)} = Transform_{2D}^c(X_{(c,x,y)}, T^{2D}) + \sum_{k=0}^{K/3-1} Slicing_{2D}^{c'+3k}(X_{(c,x,y)}, G^{2D}). \quad (10)$$

More details are provided in supplementary material.

### 3.3. Loss Function

Our loss function  $\mathcal{L}$  comprises three terms as

$$\mathcal{L} = \mathcal{L}_{mse} + \lambda_c \cdot \mathcal{L}_c + \lambda_p \cdot \mathcal{L}_p, \quad (11)$$

which are the mean squared error (MSE), color difference loss, and perceptual loss, respectively. Specifically,  $\mathcal{L}_{mse}$  calculates the MSE between predicted image  $Y$  and ground truth, which ensures the fidelity of the enhanced image.  $\mathcal{L}_c$  is the distance on the CIE94 LAB space [38], and  $\mathcal{L}_p$  is the LPIPS loss [48] on a pre-trained AlexNet [24] for the perceptual quality. Also,  $\lambda_c$  and  $\lambda_p$  are set to 0.005 and 0.05 following the previous work [22, 38], respectively.

## 4. Experiments

### 4.1. Datasets

We conduct experiments on FiveK [3] and PPR10K [28] datasets. The FiveK dataset contains 5,000 input images and five ground truths by five experts (A/B/C/D/E). The FiveK dataset consists of two types of input image formats for each task: 8-bit sRGB for photo retouch and 16-bit XYZ for tone mapping task. The ground truth has an 8-bit sRGB format that was retouched by expert C and is selected for comparison with previous LUT methods [22, 38, 43, 44, 46]. We split the dataset into 4,500 pairs for the training set and 500 pairs for the testing set, as provided split in [46]. We also use the 480p version [46] to speed up in training stage. The evaluation is carried out on 480p and 4K versions in the testing stage. The PPR10K dataset contains 11,161 RAW portrait photos with three ground truths

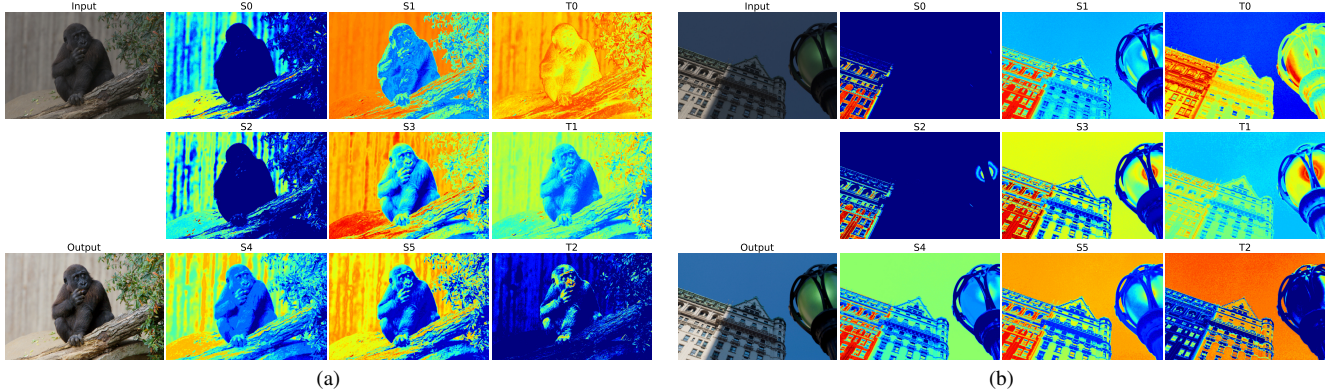


Figure 5. Visualization for results of the slicing and LUT transform. The images in the first column are input and output image, respectively. The images in the second and third columns are results of slicing operation. The images in the fourth column are results of LUT transform. The pixels closer to red indicate more activated, and the pixels closer to blue indicate less activated.

by three experts (a/b/c). Input images and ground truths have 16-bit and 8-bit sRGB formats, respectively, for photo retouch tasks. The PPR10K dataset is divided into 8,875 pairs for the training stage and 2,286 pairs for the test stage with the official split [28]. We separately conduct experiments for each ground truth on the 360p version.

## 4.2. Application Settings

We train our network in an end-to-end manner with standard Adam optimizer [23] for 400 epochs. The learning rate is initially  $1 \times 10^{-4}$  and decayed by 0.1 factor every 100 epochs. The minibatch size is 1 for FiveK and 16 for PPR10K. In the experiments on the PPR10K dataset [28], we use the ResNet-18 [14] as backbone  $B(\cdot)$  for Eq. (1) and increase the rank by a factor of 2 on LUT and weight generator for fair comparison with previous work [22, 28, 43, 44]. We implement our method on the PyTorch framework. The slicing and LUT transform operation are implemented using CUDA extension to speed up. The experiments are conducted on an NVIDIA Tesla V100 GPU except Sec. 4.6.

## 4.3. The Component-wise Ablation Study

The Tab. 6 shows a component-wise ablation study on FiveK [3]. Only Grid refers to evaluating results without the LUTs, and Only LUT does the same without the bilateral grids. “+” denotes adding LUTs or bilateral grids to match the number of parameters of the original. The results indicate using LUTs and bilateral grids separately leads to suboptimal performance. The “ $1 \times 1$  conv” denotes using  $1 \times 1$  convolution to combine the spatial features, described in Eq. (8). In conjunction with Tab. 2,  $1 \times 1$  convolution does not improve performance and inference time.

## 4.4. Analysis of Slicing and LUT Transform

In this section, we analyze the results of slicing and LUT transform. For the analysis, we visualize the results as can

be seen in Fig. 5. The results of slicing on the third column (S1, S3, S5) appear to globally adjust the input images. In the results on the second column (S0, S2, S4), specific parts of the image are highlighted that seem to help with local adjustment. Finally, the results of the LUT transform on the fourth column (T0, T1, T2) seem to adjust the correlation of colors. Each result enhances the specific part and also can be further decomposed into distinct results by three 2D LUTs or 2D bilateral grids. The weighted sum of these results provides the spatial-aware enhancement. We demonstrate that our method can handle pixel-wise spatial-aware local enhancement by this analysis.

## 4.5. Comparison with State-of-the-Arts

In this section, we compare our method with other SOTA real-time image enhancement methods [9, 12, 13, 37] and 3D LUT methods [22, 28, 43, 44, 46]. We conduct qualitative and quantitative comparisons on photo retouching and tone mapping tasks. In the case of SA-3DLUT [38] and SepLUT [44] that do not provide publicly available code, the quantitative results are referenced from their paper, and the qualitative results are not provided.

### 4.5.1. Quantitative Comparisons

We compare the methods with PSNR, SSIM [39], and  $L_2$ -distance in CIE LAB color space ( $\Delta E_{ab}$ ) for the FiveK dataset. In comparisons on PPR10K, we additionally measure the human-centered PSNR ( $PSNR^{HC}$ ) and color difference ( $\Delta E_{ab}^{HC}$ ) [28]. For runtime comparison, we measure runtime on the same image set, by running 100 times and averaging them. Tab. 3 shows that our method outperforms other methods on both resolutions. Similar results can be seen in Tab. 4 for the tone mapping task on the FiveK and Tab. 5 for the photo retouch task on the PPR10K.

Especially, our method overcomes the intrinsic problems of previous spatial-aware LUT methods, namely a tremen-

Table 3. Quantitative comparisons of photo retouch on the FiveK dataset [3]. “-” means the result is not available due to insufficient GPU memory. “\*” indicates that the results are obtained from their paper, and “/” are absent results due to publicly unavailable code. The best and second-best results are in red and blue, respectively.

Method	#param	480p				Full Resolution (4K)			
		PSNR	SSIM	$\Delta E_{ab}$	Runtime (ms)	PSNR	SSIM	$\Delta E_{ab}$	Runtime (ms)
UPE [37]	927.1K	21.88	0.853	10.80	4.27	21.65	0.859	11.09	56.88
DPE [9]	3.4M	23.75	0.908	9.34	7.21	-	-	-	-
HDRNet [12]	483.1K	24.66	0.915	8.06	3.49	24.52	0.921	8.20	56.07
DeepLPF [33]	1.7M	24.73	0.916	7.99	32.12	-	-	-	-
CSRNet [13]	36.4K	25.19	0.925	7.76	3.09	24.82	0.924	7.94	77.10
3D LUT [46]	593.5K	25.29	0.923	7.55	1.02	25.25	0.932	7.59	1.04
SA-3DLUT* [38]	4.5M	25.50	/	/	2.27	/	/	/	4.39
SepLUT* [44]	119.8K	25.47	0.921	7.54	1.10	25.43	0.932	7.56	1.20
AdaInt [43]	619.7K	25.49	0.926	7.47	1.29	25.48	0.934	7.45	1.59
SABLUT [22]	463.7K	25.66	0.930	7.29	1.20	25.66	0.937	7.27	3.64
Ours	160.5K	25.76	0.931	7.26	1.37	25.69	0.938	7.27	1.38

Table 4. Quantitative comparisons on the FiveK dataset [3] for tone mapping.

Method	480p		
	PSNR	SSIM	$\Delta E_{ab}$
UPE [37]	21.56	0.837	12.29
DPE [9]	22.93	0.894	11.09
HDRNet [12]	24.52	0.915	8.14
CSRNet [13]	25.19	0.921	7.63
3DLUT [46]	25.07	0.920	7.55
SepLUT* [44]	25.43	0.922	7.43
AdaInt [43]	25.28	0.925	7.48
SABLUT [22]	25.59	0.932	7.14
Ours	25.69	0.932	7.11

Table 6. Component-wise ablation study. “+” denotes adding LUTs or bilateral grids to match the model size of the original.

	PSNR	SSIM	$\Delta E_{ab}$	#param	FLOPs(M)
Only Grid	25.21	0.926	7.62	112.872K	81.38
Only Grid+	25.41	0.927	7.50	159.924K	154.96
Only LUT	25.49	0.929	7.44	109.332K	52.27
Only LUT+	25.53	0.930	7.41	196.380K	90.64
1×1 conv	25.68	0.929	7.32	160.508K	119.71
Ours	25.76	0.931	7.26	160.478K	110.38

dous number of parameters and a long inference time. Our method has a much smaller size than SA-3DLUT [38] (about 1/28 times) and SABLUT [22] (about 1/3 times), which is comparable with non-spatial-aware 3D LUT methods [43, 44, 46]. Furthermore, our method provides fast inference not only at 480p but also at 4K resolution.

Table 5. Quantitative comparisons on the PPR10K dataset [28] for photo retouch.

Dataset	Method	PSNR	$\Delta E_{ab}$	$PSNR^{HC}$	$\Delta E_{ab}^{HC}$
PPR10K-a	3DLUT [28]	25.64	6.97	28.89	4.53
	SepLUT* [44]	26.28	6.59	/	/
	AdaInt [43]	26.33	6.56	29.57	4.26
	SABLUT [22]	26.45	6.51	29.70	4.23
	Ours	26.50	6.46	29.74	4.20
PPR10K-b	3DLUT [28]	24.70	7.71	27.99	4.99
	SepLUT* [44]	25.23	7.49	/	/
	AdaInt [43]	25.40	7.33	28.65	4.75
	SABLUT [22]	25.48	7.19	28.72	4.66
	Ours	25.51	7.23	28.75	4.68
PPR10K-c	3DLUT [28]	25.18	7.58	28.49	4.92
	SepLUT* [44]	25.59	7.51	/	/
	AdaInt [43]	25.68	7.31	28.93	4.76
	SABLUT [22]	25.72	7.28	29.00	4.72
	Ours	25.77	7.25	29.04	4.71

Table 7. Comparisons with efficient methods with CPU (i9-12900F) and cost-effective GPU<sup>†</sup> (GTX 1660 SUPER) on the FiveK dataset [3] for photo retouch task.

Method	#param	PSNR	SSIM	$\Delta E_{ab}$	FLOPs	Runtime (ms)		
						480p		
						CPU	GPU <sup>†</sup>	4K
NILUT [10]	33.9K	21.80	0.879	10.87	11.59G	182.84	14.59	-
ICELUT [45]	299.3K	25.27	0.918	7.51	15.02M	2.93	0.76	2.75
3DLUT [46]	593.5K	25.29	0.923	7.55	92.52M	20.87	1.19	1.88
SABLUT [22]	463.7K	25.66	0.930	7.29	70.11M	26.8	1.45	11.97
Ours	160.4K	25.76	0.931	7.26	110.37M	21.71	1.64	3.94

#### 4.5.2. Qualitative Comparisons

Fig. 6 provides several qualitative comparison results with corresponding error maps on the upper right of each picture. The color of the error map represents the difference with ground truth based on the corresponding color bars on the right of each row. The comparisons in the first row

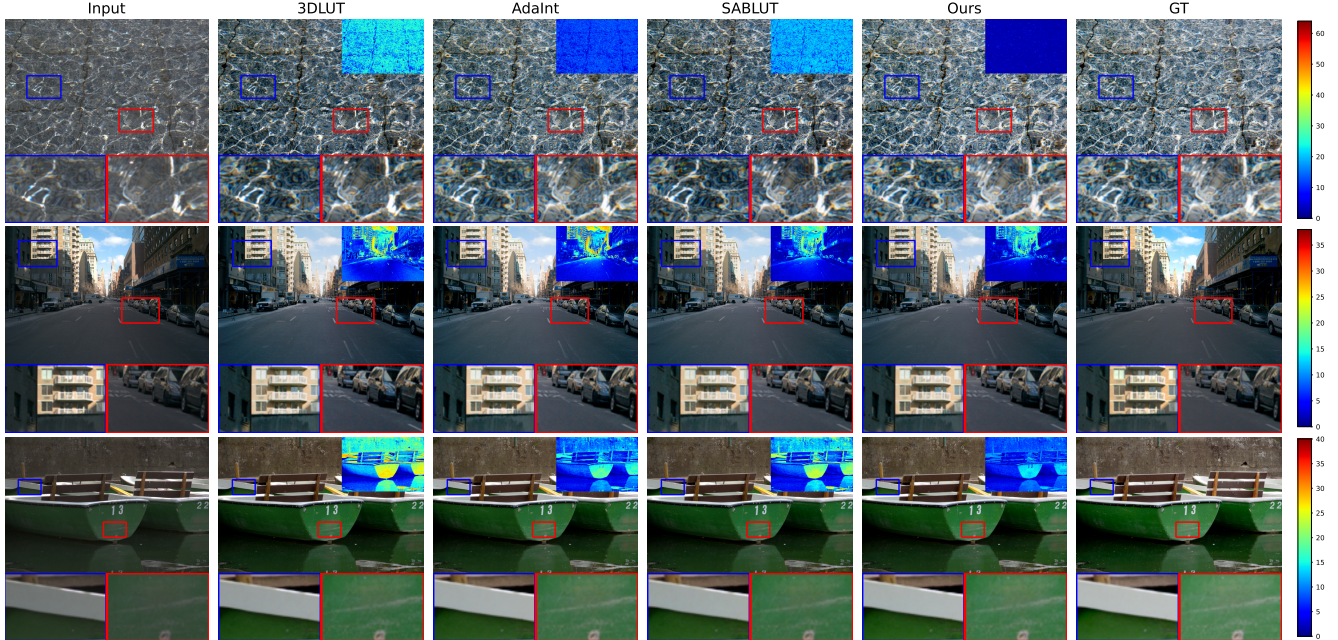


Figure 6. Qualitative comparisons for photo retouch on the FiveK dataset [3]. The corresponding error maps on the upper right of each picture indicate differences with ground truth, where each color indicates the degree of error based on the corresponding color bars.

show that our method properly handles the color and texture. Other methods produce an entirely darker color than the ground truth on both rectangles. A noticeable difference can be seen in the tile colors. Specifically, our method produces a color which is much closer to ground truth. The second row shows that spatial-aware methods (SABLUT, Ours) better handle the local enhancement than the others. Especially, our method well produces the similar color with ground truth on both dark and bright areas. The last row of the figure shows that our model has improved the overall color of the image. Specifically, the green color is closer to the ground truth than the other methods.

#### 4.6. Efficiency Analysis

The Tab. 7 shows comparisons with efficient 3D LUT methods [10, 45] on CPU (i9-12900F) and cost-effective GPU<sup>†</sup> (GTX 1660 SUPER). NILUT [10] adopts a neural implicit MLP in place of LUTs, and ICELUT [45] enhances efficiency by replacing the backbone with LUTs. Since NILUT failed to fit LUTs in 3DLUTs [46] for image-adaptiveness, we fitted NILUT to a randomly selected image. For the others, we use settings in their official repositories.

Our method performs better than the other efficient methods and has reasonable inference time on both CPU and GPU<sup>†</sup>. Although NILUT maintains a small number of parameters, its high FLOPs lead to longer inference time. ICELUT [45] achieves efficient inference time, but its lack of spatial awareness results in suboptimal performance. Although 2D LUT transform incurs an increase of FLOPs, our

method shows only a minor difference compared to 3DLUT [46] due to the shallow backbone. Furthermore, the cache-effective structure leads to a shorter inference time at 4K resolution than SABLUT [38]. When considered together with Tab. 3, we believe that the difference in inference time becomes wider as GPU performance decreases.

## 5. Discussion and Conclusion

We have developed an LUT-based image enhancement method, which decomposes the 3D LUT and 3D bilateral grid to reduce the model size and refine the spatial feature, providing a process that is cache-effective for short runtime. We demonstrated that a 3D LUT can be decomposed by a combination of 2D LUTs and SVD, achieving nearly the same performance. We modified spatial feature fusion in a cache-efficient manner, which allows us to fast processing at high resolution. We have tested our method on two benchmark datasets, showing that it performs competitively compared to other state-of-the-art methods in terms of both performance and efficiency.

While our method guarantees real-time performance on GPUs, it might not achieve the same on low-end CPUs. However, we believe that our method could be made applicable to low-end devices by adopting a shrink version as in NILUT or by replacing the backbone with LUTs, as done in ICELUT. We also believe that the decomposition method and cache-efficient structure can be applied to other frameworks. These could be directions for future work.

## Acknowledgements

This work was partly supported by Institute of Information & communications Technology Planning & Evaluation (IITP) grant funded by the Korea government(MSIT) [NO.RS-2021-II211343, Artificial Intelligence Graduate School Program (Seoul National University)] and the BK21 FOUR program of the Education and Research Program for Future ICT Pioneers, Seoul National University in 2025.

## References

- [1] SM A Sharif, Rizwan Ali Naqvi, Mithun Biswas, and Sungjun Kim. A two-stage deep network for high dynamic range image reconstruction. In *Proceedings of the IEEE/CVF Conference on Computer Vision and Pattern Recognition*, pages 550–559, 2021. 1
- [2] Ahmet Oğuz Akyüz et al. Deep joint deinterlacing and denoising for single shot dual-iso hdr reconstruction. *IEEE Transactions on Image Processing*, 29:7511–7524, 2020. 1
- [3] Vladimir Bychkovsky, Sylvain Paris, Eric Chan, and Frédo Durand. Learning photographic global tonal adjustment with a database of input/output image pairs. In *CVPR 2011*, pages 97–104. IEEE, 2011. 1, 3, 4, 5, 6, 7, 8, 12, 15, 16
- [4] Jianrui Cai, Shuhang Gu, and Lei Zhang. Learning a deep single image contrast enhancer from multi-exposure images. *IEEE Transactions on Image Processing*, 27(4):2049–2062, 2018. 1
- [5] Chen Chen, Qifeng Chen, Jia Xu, and Vladlen Koltun. Learning to see in the dark. In *Proceedings of the IEEE conference on computer vision and pattern recognition*, pages 3291–3300, 2018. 1
- [6] Jiawen Chen, Sylvain Paris, and Frédo Durand. Real-time edge-aware image processing with the bilateral grid. *ACM Transactions on Graphics (TOG)*, 26(3):103–es, 2007. 4
- [7] Jiawen Chen, Andrew Adams, Neal Wadhwa, and Samuel W Hasinoff. Bilateral guided upsampling. *ACM Transactions on Graphics (TOG)*, 35(6):1–8, 2016.
- [8] Xiangyu Chen, Yihao Liu, Zhengwen Zhang, Yu Qiao, and Chao Dong. Hdrnet: Single image hdr reconstruction with denoising and dequantization. In *Proceedings of the IEEE/CVF Conference on Computer Vision and Pattern Recognition*, pages 354–363, 2021. 1
- [9] Yu-Sheng Chen, Yu-Ching Wang, Man-Hsin Kao, and Yung-Yu Chuang. Deep photo enhancer: Unpaired learning for image enhancement from photographs with gans. In *Proceedings of the IEEE conference on computer vision and pattern recognition*, pages 6306–6314, 2018. 1, 6, 7
- [10] Marcos V Conde, Javier Vazquez-Corral, Michael S Brown, and Radu Timofte. Nilut: Conditional neural implicit 3d lookup tables for image enhancement. In *Proceedings of the AAAI Conference on Artificial Intelligence*, pages 1371–1379, 2024. 7, 8
- [11] Yubin Deng, Chen Change Loy, and Xiaoou Tang. Aesthetic-driven image enhancement by adversarial learning. In *Proceedings of the 26th ACM international conference on Multimedia*, pages 870–878, 2018. 1
- [12] Michaël Gharbi, Jiawen Chen, Jonathan T Barron, Samuel W Hasinoff, and Frédo Durand. Deep bilateral learning for real-time image enhancement. *ACM Transactions on Graphics (TOG)*, 36(4):1–12, 2017. 6, 7, 15
- [13] Jingwen He, Yihao Liu, Yu Qiao, and Chao Dong. Conditional sequential modulation for efficient global image retouching. In *Computer Vision–ECCV 2020: 16th European Conference, Glasgow, UK, August 23–28, 2020, Proceedings, Part XIII 16*, pages 679–695. Springer, 2020. 6, 7, 15
- [14] Kaiming He, Xiangyu Zhang, Shaoqing Ren, and Jian Sun. Deep residual learning for image recognition. In *Proceedings of the IEEE conference on computer vision and pattern recognition*, pages 770–778, 2016. 6
- [15] Yuanming Hu, Hao He, Chenxi Xu, Baoyuan Wang, and Stephen Lin. Exposure: A white-box photo post-processing framework. *ACM Transactions on Graphics (TOG)*, 37(2):1–17, 2018.
- [16] Xin Huang, Qi Zhang, Ying Feng, Hongdong Li, Xuan Wang, and Qing Wang. Hdr-nerf: High dynamic range neural radiance fields. In *Proceedings of the IEEE/CVF Conference on Computer Vision and Pattern Recognition*, pages 18398–18408, 2022. 1
- [17] Andrey Ignatov, Nikolay Kobyshev, Radu Timofte, Kenneth Vanhoey, and Luc Van Gool. Dslr-quality photos on mobile devices with deep convolutional networks. In *Proceedings of the IEEE international conference on computer vision*, pages 3277–3285, 2017.
- [18] Yifan Jiang, Xinyu Gong, Ding Liu, Yu Cheng, Chen Fang, Xiaohui Shen, Jianchao Yang, Pan Zhou, and Zhangyang Wang. Enlightengan: Deep light enhancement without paired supervision. *IEEE transactions on image processing*, 30:2340–2349, 2021. 1
- [19] Younghyun Jo and Seon Joo Kim. Practical single-image super-resolution using look-up table. In *Proceedings of the IEEE/CVF Conference on Computer Vision and Pattern Recognition (CVPR)*, pages 691–700, 2021. 1
- [20] Han-Ul Kim, Young Jun Koh, and Chang-Su Kim. Pienet: Personalized image enhancement network. In *Computer Vision–ECCV 2020: 16th European Conference, Glasgow, UK, August 23–28, 2020, Proceedings, Part XXX 16*, pages 374–390. Springer, 2020. 1
- [21] Soo Ye Kim, Jihyong Oh, and Munchurl Kim. Jsi-gan: Gan-based joint super-resolution and inverse tone-mapping with pixel-wise task-specific filters for uhd hdr video. In *Proceedings of the AAAI Conference on Artificial Intelligence*, pages 11287–11295, 2020. 1
- [22] Wontae Kim and Nam Ik Cho. Image-adaptive 3d lookup tables for real-time image enhancement with bilateral grids. In *European Conference on Computer Vision*, pages 91–108, 2024. 1, 2, 3, 4, 5, 6, 7, 12, 15
- [23] Diederik P Kingma and Jimmy Ba. Adam: A method for stochastic optimization. *arXiv preprint arXiv:1412.6980*, 2014. 6
- [24] Alex Krizhevsky, Ilya Sutskever, and Geoffrey E Hinton. Imagenet classification with deep convolutional neural networks. *Advances in neural information processing systems*, 25, 2012. 5

- [25] Phuoc-Hieu Le, Quynh Le, Rang Nguyen, and Binh-Son Hua. Single-image hdr reconstruction by multi-exposure generation. In *Proceedings of the IEEE/CVF Winter Conference on Applications of Computer Vision*, pages 4063–4072, 2023. 1
- [26] Jiacheng Li, Chang Chen, Zhen Cheng, and Zhiwei Xiong. Mulut: Cooperating multiple look-up tables for efficient image super-resolution. In *European conference on computer vision*, pages 238–256. Springer, 2022. 1
- [27] Yinglong Li, Jiacheng Li, and Zhiwei Xiong. Look-up table compression for efficient image restoration. In *Proceedings of the IEEE/CVF Conference on Computer Vision and Pattern Recognition (CVPR)*, pages 26016–26025, 2024. 1, 2
- [28] Jie Liang, Hui Zeng, Miaomiao Cui, Xuansong Xie, and Lei Zhang. Ppr10k: A large-scale portrait photo retouching dataset with human-region mask and group-level consistency. In *Proceedings of the IEEE/CVF Conference on Computer Vision and Pattern Recognition*, pages 653–661, 2021. 1, 2, 4, 5, 6, 7, 12, 15, 17
- [29] Chengxu Liu, Huan Yang, Jianlong Fu, and Xueming Qian. 4d lut: learnable context-aware 4d lookup table for image enhancement. *IEEE Transactions on Image Processing*, 32: 4742–4756, 2023. 1, 2
- [30] Guandu Liu, Yukang Ding, Mading Li, Ming Sun, Xing Wen, and Bin Wang. Reconstructed convolution module based look-up tables for efficient image super-resolution. In *Proceedings of the IEEE/CVF international conference on computer vision*, pages 12217–12226, 2023. 1
- [31] Yu-Lun Liu, Wei-Sheng Lai, Yu-Sheng Chen, Yi-Lung Kao, Ming-Hsuan Yang, Yung-Yu Chuang, and Jia-Bin Huang. Single-image hdr reconstruction by learning to reverse the camera pipeline. In *Proceedings of the IEEE/CVF Conference on Computer Vision and Pattern Recognition*, pages 1651–1660, 2020. 1
- [32] Cheng Ma, Jingyi Zhang, Jie Zhou, and Jiwen Lu. Learning series-parallel lookup tables for efficient image super-resolution. In *European Conference on Computer Vision*, pages 305–321. Springer, 2022. 1
- [33] Sean Moran, Pierre Marza, Steven McDonagh, Sarah Parisot, and Gregory Slabaugh. Deeplpf: Deep local parametric filters for image enhancement. In *Proceedings of the IEEE/CVF conference on computer vision and pattern recognition*, pages 12826–12835, 2020. 1, 7
- [34] Jongchan Park, Joon-Young Lee, Donggeun Yoo, and In So Kweon. Distort-and-recover: Color enhancement using deep reinforcement learning. In *Proceedings of the IEEE conference on computer vision and pattern recognition*, pages 5928–5936, 2018.
- [35] Olaf Ronneberger, Philipp Fischer, and Thomas Brox. U-net: Convolutional networks for biomedical image segmentation. In *Medical Image Computing and Computer-Assisted Intervention—MICCAI 2015: 18th International Conference, Munich, Germany, October 5-9, 2015, Proceedings, Part III 18*, pages 234–241. Springer, 2015. 2
- [36] Jean D Vandenberg and Stefano Andriani. A survey on 3d-lut performance in 10-bit and 12-bit hdr bt. 2100 pq. In *SMPTE 2018*, pages 1–19. SMPTE, 2018. 3
- [37] Ruixing Wang, Qing Zhang, Chi-Wing Fu, Xiaoyong Shen, Wei-Shi Zheng, and Jiaya Jia. Underexposed photo enhancement using deep illumination estimation. In *Proceedings of the IEEE/CVF conference on computer vision and pattern recognition*, pages 6849–6857, 2019. 6, 7
- [38] Tao Wang, Yong Li, Jingyang Peng, Yipeng Ma, Xian Wang, Fenglong Song, and Youliang Yan. Real-time image enhancer via learnable spatial-aware 3d lookup tables. In *Proceedings of the IEEE/CVF International Conference on Computer Vision (ICCV)*, pages 2471–2480, 2021. 1, 2, 5, 6, 7, 8, 12
- [39] Zhou Wang, Alan C Bovik, Hamid R Sheikh, and Eero P Simoncelli. Image quality assessment: from error visibility to structural similarity. *IEEE transactions on image processing*, 13(4):600–612, 2004. 6
- [40] Chen Wei, Wenjing Wang, Wenhan Yang, and Jiaying Liu. Deep retinex decomposition for low-light enhancement. *arXiv preprint arXiv:1808.04560*, 2018. 1
- [41] Bin Xu, Yuhua Xu, Xiaoli Yang, Wei Jia, and Yulan Guo. Bilateral grid learning for stereo matching networks. In *Proceedings of the IEEE/CVF Conference on Computer Vision and Pattern Recognition*, pages 12497–12506, 2021.
- [42] Zhicheng Yan, Hao Zhang, Baoyuan Wang, Sylvain Paris, and Yizhou Yu. Automatic photo adjustment using deep neural networks. *ACM Transactions on Graphics (TOG)*, 35(2): 1–15, 2016. 1
- [43] Canqian Yang, Meiguang Jin, Xu Jia, Yi Xu, and Ying Chen. Adaint: Learning adaptive intervals for 3d lookup tables on real-time image enhancement. In *Proceedings of the IEEE/CVF Conference on Computer Vision and Pattern Recognition (CVPR)*, pages 17522–17531, 2022. 1, 2, 5, 6, 7, 12, 15
- [44] Canqian Yang, Meiguang Jin, Yi Xu, Rui Zhang, Ying Chen, and Huaida Liu. Seplut: Separable image-adaptive lookup tables for real-time image enhancement. In *European Conference on Computer Vision (ECCV)*, pages 201–217. Springer, 2022. 2, 3, 5, 6, 7, 12
- [45] Sidi Yang, Binxiao Huang, Mingdeng Cao, Yatai Ji, Hanzhong Guo, Ngai Wong, and Yujiu Yang. Taming lookup tables for efficient image retouching. In *European Conference on Computer Vision*, pages 144–159. Springer, 2024. 7, 8
- [46] Hui Zeng, Jianrui Cai, Lida Li, Zisheng Cao, and Lei Zhang. Learning image-adaptive 3d lookup tables for high performance photo enhancement in real-time. *IEEE Transactions on Pattern Analysis and Machine Intelligence (TPAMI)*, 44(4):2058–2073, 2022. 1, 2, 5, 6, 7, 8, 12, 15
- [47] Fengyi Zhang, Hui Zeng, Tianjun Zhang, and Lin Zhang. Clut-net: Learning adaptively compressed representations of 3dluts for lightweight image enhancement. In *Proceedings of the 30th ACM International Conference on Multimedia*, pages 6493–6501, 2022. 1, 2
- [48] Richard Zhang, Phillip Isola, Alexei A Efros, Eli Shechtman, and Oliver Wang. The unreasonable effectiveness of deep features as a perceptual metric. In *Proceedings of the IEEE conference on computer vision and pattern recognition*, pages 586–595, 2018. 5

- [49] Yonghua Zhang, Jiawan Zhang, and Xiaojie Guo. Kindling the darkness: A practical low-light image enhancer. In *Proceedings of the 27th ACM international conference on multimedia*, pages 1632–1640, 2019. [1](#)
- [50] Zhuoran Zheng, Wenqi Ren, Xiaochun Cao, Xiaobin Hu, Tao Wang, Fenglong Song, and Xiuyi Jia. Ultra-high-definition image dehazing via multi-guided bilateral learning. In *2021 IEEE/CVF Conference on Computer Vision and Pattern Recognition (CVPR)*, pages 16180–16189. IEEE, 2021.
- [51] Zhuoran Zheng, Wenqi Ren, Xiaochun Cao, Tao Wang, and Xiuyi Jia. Ultra-high-definition image hdr reconstruction via collaborative bilateral learning. In *Proceedings of the IEEE/CVF international conference on computer vision*, pages 4449–4458, 2021.
- [52] Yijie Zhou, Chao Li, Jin Liang, Tianyi Xu, Xin Liu, and Jun Xu. 4k-resolution photo exposure correction at 125 fps with 8k parameters. In *Proceedings of the IEEE/CVF Winter Conference on Applications of Computer Vision*, pages 1587–1597, 2024.
- [53] Rafat Mantiuk, Kil Joong Kim, Allan G Rempel, and Wolfgang Heidrich. Hdr-vdp-2: A calibrated visual metric for visibility and quality predictions in all luminance conditions. *ACM Transactions on graphics (TOG)*, 30(4):1–14, 2011. [15](#)
- [54] Xiangyu Chen, Zhengwen Zhang, Jimmy S Ren, Lynhoo Tian, Yu Qiao, and Chao Dong. A new journey from sdr tv to hdr tv. In *Proceedings of the IEEE/CVF International Conference on Computer Vision*, pages 4500–4509, 2021. [15](#), [18](#)
- [55] ITU-R. Objective metric for the assessment of the potential visibility of colour differences in television. ITU-R Rec BT.2124-0, 2019. [15](#)

# Lightweight and Fast Real-time Image Enhancement via Decomposition of the Spatial-aware Lookup Tables

## Supplementary Material

In this supplementary material, we provide the following.

- Appendix A Details of network structure.
- Appendix B Analysis for PPR10K Dataset.
- Appendix C Details of 2D slicing and LUT transform.
- Appendix D Additional quantitative and qualitative comparisons.

### A. Details of Network Structure

In this section, we provide the details of our network structure as described in Tabs. 8 to 12. The backbone in Tab. 8 consists of five layers of a convolutional neural network (CNN), with  $m$  set to 8, following previous work [22]. Each generator in Tabs. 9 to 12 is composed of two fully connected (FC) layers with the insight of rank factorization, which can reduce the parameters and training difficulty [22, 43, 44]. The bilateral grid generator  $H_s(\cdot)$  in Tab. 9 generates 2D bilateral grids to replace 3D bilateral grids. We decide the  $D_s = 17$ ,  $K = 6$  for fair comparison on spatial feature fusion with SABLUT [22]. The weights and biases for 2D bilateral grids are generated by the bilateral grid weight generator  $H_{sw}(\cdot)$  in Tab. 10. We experimentally select the number of hidden layers for the bilateral grid weight generator as  $M_{sw} = 8$ . Since three 2D bilateral grids replace a 3D bilateral grid, the number of weights  $N_{sw}$  and biases  $N_{sb}$  for each channel are 3 and 1, respectively.

The LUT generator  $H_t(\cdot)$  in Tab. 11 generates the singular value decomposition (SVD) components of 2D LUTs with eight singular values  $N_s = 8$  as described in the main paper. Most of previous 3D LUT methods [22, 28, 38, 43, 44, 46] have  $D_t = 17$  or  $D_t = 33$  vertices. When we set  $D_t$  to 17, our model does not achieve the desired performance, with a PSNR of 25.54 dB on the photo retouch task on FiveK [3]. Meanwhile, our method achieves a competitive performance of 25.76 dB with  $D_t = 33$  in the same task. We decide to set  $D_t$  as 33, based on the above experiment. The 2D LUTs can be easily reconstructed by matrix multiplication, as discussed in the main paper. The LUT weight generator  $H_{tw}(\cdot)$  in Tab. 12 is similar to the bilateral grid weight generator. The parameters of the LUT weight generator,  $M_{tw} = 8$ ,  $N_{tw} = 3$ , and  $N_{tb} = 1$ , are decided for the same reason as the bilateral grid weight generator.

### B. Analysis for PPR10K Datasets

We also conduct an analysis for PPR10K on utilization rates and occurrence statistics. The utilization rate indicates how

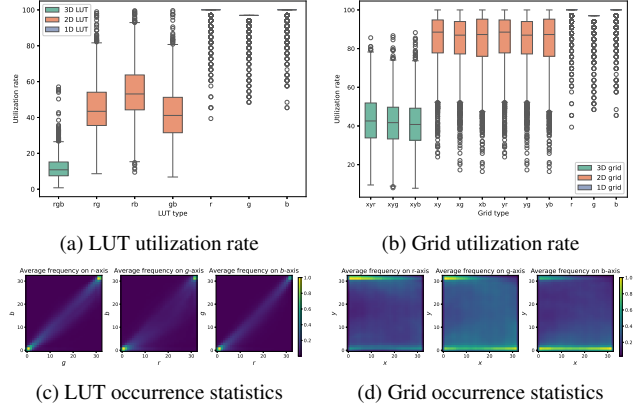


Figure 7. (a) and (b) are box plots of utilization rates on PPR10K dataset [28] under different dimensions of LUT and bilateral grid. Each color represents the dimension of LUT and bilateral grid. (c) and (d) are LUT visualizations of average occurrence statistics on each axis for PPR10K. The cells closer to yellow indicate more frequently accessed vertices and the cells closer to blue indicate less frequently accessed vertices.

many vertices of a 3D LUT are referenced compared to generated vertices for each image, like  $\frac{\#referenced\ vertices}{\#generated\ vertices} \times 100$ . The occurrence statistics are estimated by counting the number of accesses for each vertex. The overall tendency is similar to the results of the analysis for FiveK in the main paper. Fig. 7a presents LUT utilization rate of PPR10K. The rate of 3D LUT is very low, and 1D LUT is saturated. As can be seen in Fig. 7c, the occurrence statistics are concentrated on the diagonal. Notably, the vertices near (1,1) and (32,32) are accessed more frequently than other diagonal vertices, compared to the FiveK dataset. The bilateral grid has a broader distribution than LUT, but it also has a similar tendency. The 3D bilateral grid is redundant, and the 1D bilateral grid is saturated, similar to the FiveK dataset, as shown in Fig. 7b. The vertices access is concentrated on as visualized in the first row and the thirty-second row in Fig. 7d.

### C. Details of 2D Slicing and LUT Transform

In this section, we provide a detailed description of the 2D LUT Transform and 2D Slicing.

#### C.1. 2D LUT Transform

Fig. 8a illustrates the detailed operation of 2D LUT transform  $Transform_{2D}^c(X_{(c,x,y)}, T^{2D})$  based on bilinear in-

Table 8. Details of the backbone network  $B(\cdot)$  where  $Conv3$  is  $3 \times 3$  convolution block (stride=2, padding=1),  $LR$  is LeakyReLU and  $IN$  is instance normalization.

Layer	Output Shape
Bilinear Downsample	$3 \times 256 \times 256$
$Conv3 + LR + IN$	$m \times 128 \times 128$
$Conv3 + LR + IN$	$2m \times 64 \times 64$
$Conv3 + LR + IN$	$4m \times 32 \times 32$
$Conv3 + LR + IN$	$8m \times 16 \times 16$
$Conv3 + LR$	$8m \times 8 \times 8$
Droupout (0.5)	$8m \times 8 \times 8$
Average Pooling	$8m \times 2 \times 2$
Reshape	$32m$

Table 9. Details of the bilateral grid generator  $H_s(\cdot)$ , where  $FC$  is a fully connected layer.  $M_s$ ,  $K$ , and  $D_s$  are the number of hidden layers, bilateral grids, and bilateral grid vertices, respectively.

Layer	Output Shape
$FC$	$M_s$
$FC$	$K \cdot 3 \cdot D_s^2$
Reshape	$K \times 3 \times D_s \times D_s$

Table 11. Details of the LUT generator  $H_t(\cdot)$ .  $M_t$ ,  $D_t$  and  $N_S$  are the number of hidden layers, LUT vertices, and singular values, respectively.

Layer	Output Shape
$FC$	$M_t$
$FC$	$3 \cdot 3 \cdot (D_t \cdot N_S + N_S + D_t \cdot N_S)$
	$U : 3 \times 3 \times (D_t \times N_S)$
Reshape	$S : 3 \times 3 \times N_S$
	$V : 3 \times 3 \times (D_t \times N_S)$

Table 10. Details of the bilateral grid weight generator  $H_{sw}(\cdot)$ .  $M_{sw}$  is the number of hidden layers.  $N_{sw}$  and  $N_{sb}$  are the number of bilateral grid weights and biases for each channel, respectively.

Layer	Output Shape
$FC$	$M_{sw}$
$FC$	$K \cdot 3 \cdot (N_{sw} + N_{sb})$
Reshape	$K \times 3 \times (N_{sw} + N_{sb})$

Table 12. Details of the LUT weight generator  $H_{tw}(\cdot)$ .  $M_{tw}$  are the number of hidden layers.  $N_{tw}$  and  $N_{tb}$  are the number of LUT weights and biases for each channel, respectively.

Layer	Output Shape
$FC$	$M_{tw}$
$FC$	$3 \cdot 3 \cdot (N_{tw} + N_{tb})$
Reshape	$3 \times 3 \times (N_{tw} + N_{tb})$

terpolation, where  $T^{2D} \in \{t_{rg}^c, t_{rb}^c, t_{gb}^c | c \in \{r, g, b\}\}$  represents 2D LUTs and  $X_{(c,x,y)}$  is the pixel value on  $(c, x, y)$ . The 2D LUT transform comprises the following three steps. First of all, query points for 2D LUTs are found based on input color values, which can be described as

$$\begin{aligned} P_{rg} &= (p_r, p_g) = (X_{(r,x,y)}, X_{(g,x,y)}), \\ P_{rb} &= (p_r, p_b) = (X_{(r,x,y)}, X_{(b,x,y)}), \\ P_{gb} &= (p_g, p_b) = (X_{(g,x,y)}, X_{(b,x,y)}), \end{aligned} \quad (12)$$

where  $P_{rg}$ ,  $P_{rb}$ , and  $P_{gb}$  are query points for  $t_{rg}^c$ ,  $t_{rb}^c$ , and  $t_{gb}^c$ , respectively.

Second, the bilinear interpolation is carried out to calculate retrieved values  $\phi_{\alpha\beta}^c$  from  $t_{\alpha\beta}^c$  with  $\alpha\beta \in \{rg, rb, gb\}$ . For the interpolation operation, we find the left and right vertices of each query point on their axis. The left and right vertices can be denoted as

$$\begin{aligned} p_\alpha^l &= \lfloor p_\alpha \cdot (D_t - 1) \rfloor / (D_t - 1), \\ p_\alpha^r &= p_\alpha^l + 1 / (D_t - 1), \\ p_\beta^l &= \lfloor p_\beta \cdot (D_t - 1) \rfloor / (D_t - 1), \\ p_\beta^r &= p_\beta^l + 1 / (D_t - 1), \end{aligned} \quad (13)$$

where  $\lfloor \cdot \rfloor$  is floor operator. The four adjacent points on a 2D LUT can be found as

$$\begin{aligned} V_{\alpha\beta}^{c,00} &= t_{\alpha\beta}^c(p_\alpha^l, p_\beta^l), \\ V_{\alpha\beta}^{c,10} &= t_{\alpha\beta}^c(p_\alpha^r, p_\beta^l), \\ V_{\alpha\beta}^{c,01} &= t_{\alpha\beta}^c(p_\alpha^l, p_\beta^r), \\ V_{\alpha\beta}^{c,11} &= t_{\alpha\beta}^c(p_\alpha^r, p_\beta^r). \end{aligned} \quad (14)$$

The retrieved values can be calculated by bilinear interpolation, which can be formulated as

$$\begin{aligned} \phi_{\alpha\beta,(x,y)}^c &= (1 - \delta_\alpha) \cdot (1 - \delta_\beta) \cdot V_{\alpha\beta}^{c,00} \\ &+ \delta_\alpha \cdot (1 - \delta_\beta) \cdot V_{\alpha\beta}^{c,10} \\ &+ (1 - \delta_\alpha) \cdot \delta_\beta \cdot V_{\alpha\beta}^{c,01} \\ &+ \delta_\alpha \cdot \delta_\beta \cdot V_{\alpha\beta}^{c,11}, \end{aligned} \quad (15)$$

where  $\delta_\alpha = (p_\alpha - p_\alpha^l) / (p_\alpha^r - p_\alpha^l)$  and  $\delta_\beta = (p_\beta - p_\beta^l) / (p_\beta^r - p_\beta^l)$ .

Finally, the weighted sum is conducted to calculate output values  $\Phi^c$  of a 2D LUT transform like

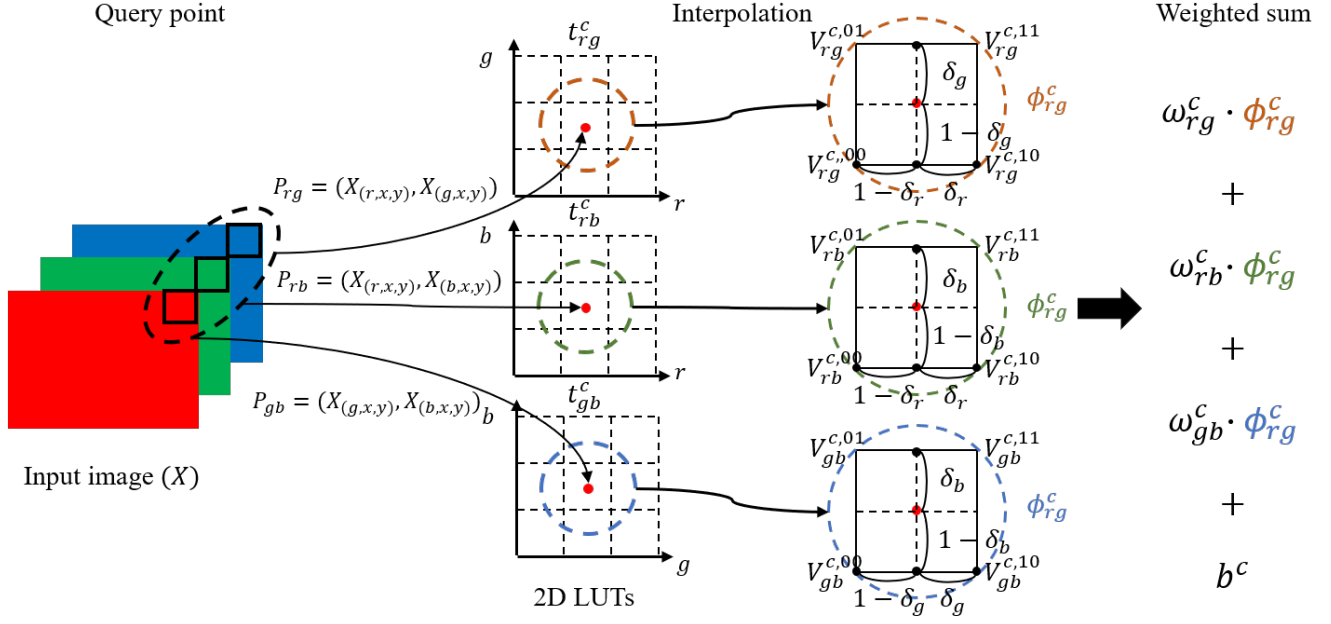
$$\begin{aligned} \Phi_{(x,y)}^c &= w_{rg}^c \cdot \phi_{rg,(x,y)}^c \\ &+ w_{rb}^c \cdot \phi_{rb,(x,y)}^c \\ &+ w_{rb}^c \cdot \phi_{rb,(x,y)}^c + b^c, \end{aligned} \quad (16)$$

where  $w_{rg}^c$ ,  $w_{rb}^c$ ,  $w_{gb}^c$ , and  $b^c$  are generated weights by LUT weight generator  $H_{tw}(\cdot)$  in Appendix A.

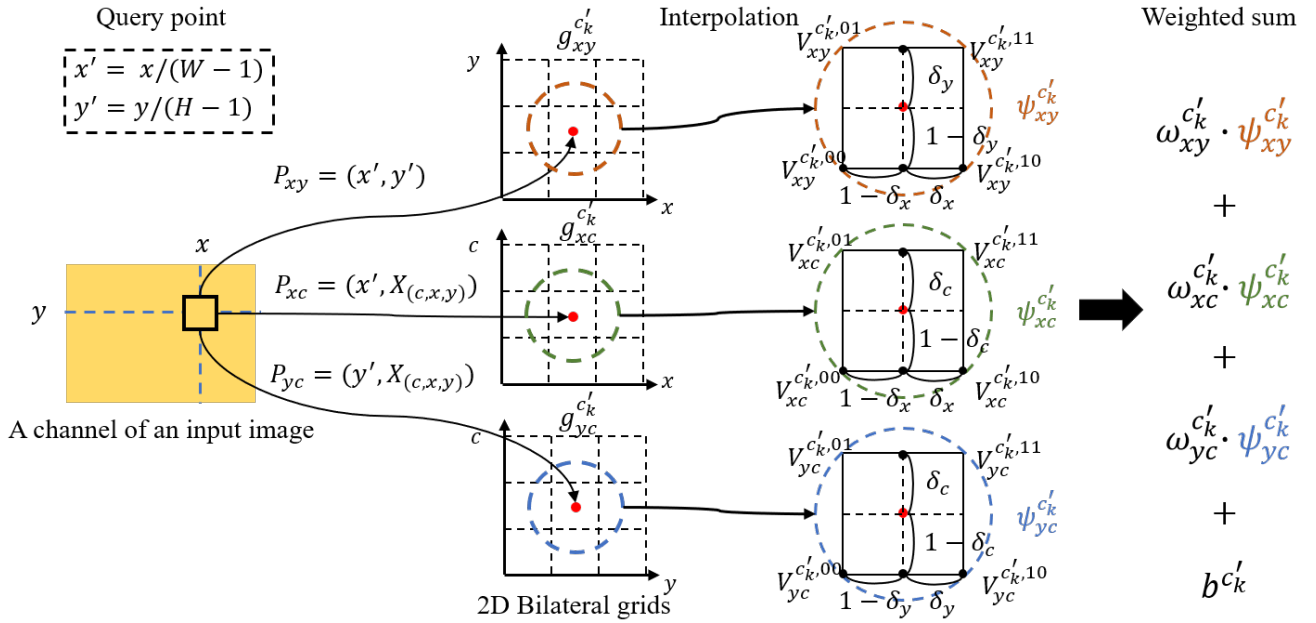
## C.2. 2D Slicing

As can be seen in Fig. 8b, the 2D slicing operation  $Slicing_{2D}^k(X, G^{2D})$  is similar to the LUT transform since both operations are based on bilinear interpolation. First, we find the query points based on the spatial coordinate  $(x, y)$  and the corresponding color value on each channel of the image, which can be denoted as

$$\begin{aligned} P_{xy} &= (p_x, p_y) = (x', y'), \\ P_{xc} &= (p_x, p_c) = (x', X_{(c'_k, x, y)}), \\ P_{yc} &= (p_y, p_c) = (y', X_{(c'_k, x, y)}), \end{aligned} \quad (17)$$



(a) Description of the 2D LUT transform



(b) Description of the 2D slicing

Figure 8. Detailed description of 2D LUT transform (a) and 2D Slicing (b) based on bilinear interpolation.

where  $x' = x/(W - 1)$ ,  $y' = y/(H - 1)$  and  $k' = \text{mod}(k, 3)$ .

Second, the bilinear interpolation is also carried out on 2D bilateral grids  $g_{\alpha\beta}^{c'_k}$  for retrieved values  $\psi_{\alpha\beta}^{c'_k}$  with  $\alpha\beta \in \{xy, xc, yc\}$ . The neighboring vertices and adjacent points

of each query point for slicing can be defined as

$$\begin{aligned} p_\alpha^l &= \lfloor p_\alpha \cdot (D_s - 1) \rfloor / (D_s - 1), \\ p_\alpha^r &= p_\alpha^l + 1 / (D_s - 1), \\ p_\beta^l &= \lfloor p_\beta \cdot (D_s - 1) \rfloor / (D_s - 1), \\ p_\beta^r &= p_\beta^l + 1 / (D_s - 1), \end{aligned} \quad (18)$$

$$\begin{aligned}
V_{\alpha\beta}^{c'_k,00} &= g_{\alpha\beta}^{c'_k}(p_\alpha^l, p_\beta^l), \\
V_{\alpha\beta}^{c'_k,10} &= g_{\alpha\beta}^{c'_k}(p_\alpha^r, p_\beta^l), \\
V_{\alpha\beta}^{c'_k,01} &= g_{\alpha\beta}^{c'_k}(p_\alpha^l, p_\beta^r), \\
V_{\alpha\beta}^{c'_k,11} &= g_{\alpha\beta}^{c'_k}(p_\alpha^r, p_\beta^r).
\end{aligned} \tag{19}$$

The retrieved values by slicing can be formulated as

$$\begin{aligned}
\psi_{\alpha\beta,(x,y)}^{c'_k} &= (1 - \delta_\alpha) \cdot (1 - \delta_\beta) \cdot V_{\alpha\beta}^{c'_k,00} \\
&+ \delta_\alpha \cdot (1 - \delta_\beta) \cdot V_{\alpha\beta}^{c'_k,10} \\
&+ (1 - \delta_\alpha) \cdot \delta_\beta \cdot V_{\alpha\beta}^{c'_k,01} \\
&+ \delta_\alpha \cdot \delta_\beta \cdot V_{\alpha\beta}^{c'_k,11}.
\end{aligned} \tag{20}$$

Finally, output values  $\Psi^{c'_k}$  of 2D slicing can be calculated through a weighted sum with generated weights by the bilateral grid weight generator  $H_{sw}(\cdot)$  in Appendix A. The weighted sum can be denoted as

$$\begin{aligned}
\Psi_{(x,y)}^{c'_k} &= w_{xy}^{c'_k} \cdot \psi_{xy,(x,y)}^{c'_k} \\
&+ w_{xc}^{c'_k} \cdot \psi_{xc,(x,y)}^{c'_k} \\
&+ w_{yc}^{c'_k} \cdot \psi_{yc,(x,y)}^{c'_k} + b^{c'_k}.
\end{aligned} \tag{21}$$

### C.3. Slicing and LUT Transform

Using notations in previous sections, the cache-effective slicing and LUT transform in the main paper can be rewritten as

$$\begin{aligned}
Y_{(r,x,y)} &= \Phi_{(x,y)}^r + \sum_{k=0}^{K/3-1} \Psi_{(x,y)}^{3k}, \\
Y_{(g,x,y)} &= \Phi_{(x,y)}^g + \sum_{k=0}^{K/3-1} \Psi_{(x,y)}^{1+3k}, \\
Y_{(b,x,y)} &= \Phi_{(x,y)}^b + \sum_{k=0}^{K/3-1} \Psi_{(x,y)}^{2+3k}.
\end{aligned} \tag{22}$$

## D. Additional Quantitative and Qualitative Comparisons

In this section, we provide additional quantitative comparisons on HDRTV1K dataset [54]. Additional qualitative comparisons are conducted on FiveK [3], PPR10K [28], and HDRTV1K [54].

### D.1. Additional Dataset

The HDRTV1K is a dataset for the SDRTV-to-HDRTV task, which converts SDR contents to their HDRTV version. This dataset comprises captured images from 22

HDR10 videos and their corresponding SDR versions. All HDR10 videos are encoded using PQ-OETF and the rec.2020 gamut. The 1235 images from 18 videos are used in the training stage, and 117 images from 4 videos are used in the testing stage.

Table 13. Quantitative comparisons on HDRTV1K [54]. The best and second-best results are in red and blue, respectively.

Method	PSNR	SSIM	$\Delta E_{ITP}$	HDR-VPD3	Runtime(ms)
HDRNet [12]	35.73	<b>0.9664</b>	11.52	8.462	56.07
CSRNet [13]	35.04	0.9625	14.28	8.400	77.1
3DLUT [46]	36.06	0.9609	10.73	8.353	<b>1.04</b>
AdaInt [43]	36.22	0.9658	10.89	8.423	1.59
SABLUT [22]	36.41	0.9657	10.28	8.460	3.64
HDRTVNet [54]	<b>36.88</b>	0.9655	<b>9.78</b>	<b>8.464</b>	70.01
Ours	<b>36.74</b>	<b>0.9663</b>	<b>9.99</b>	<b>8.500</b>	<b>1.38</b>

### D.2. Additional Quantitative Comparisons

We compare our method with other SOTA real-time methods [12, 13, 22, 43, 46] and HDRTVNet [54] on the HDRTV1K [54]. HDRTVNet is a method for the SDRTV-to-HDRTV task, which is introduced together with the HDRTV1K dataset in their paper [54]. HDRTVNet is set to the fastest configuration to compare the real-time performance, which only uses the adaptive global color mapping.

We measure PSNR, SSIM,  $\Delta E_{ITP}$  [55], and HDR-VPD3 [53]. The  $\Delta E_{ITP}$  is the color difference on the ICtCp space and is designed for HDRTV. HDR-VPD3 is an improved version of HDR-VPD2 that supports the rec.2020 gamut. We measure these metrics using codes in the official repository of HDRNet. As the HDRTV1K dataset was captured from video sequences, this experiment can offer insights into the performance on video.

As can be seen in Tab. 13, our method shows suitable performance and inference time on real-time video processing. Although HDRTVNet has the best score on PSNR and  $\Delta E_{ITP}$ , it fails to achieve real-time performance under the fastest configuration. Our model delivers real-time processing with a minor performance drop: 0.11 dB on PSNR, 0.0001 on SSIM, and 0.11 on  $\Delta E_{ITP}$ .

### D.3. Additional Qualitative Comparisons

We provide additional qualitative results in Fig. 9, Fig. 10 and Fig. 11.

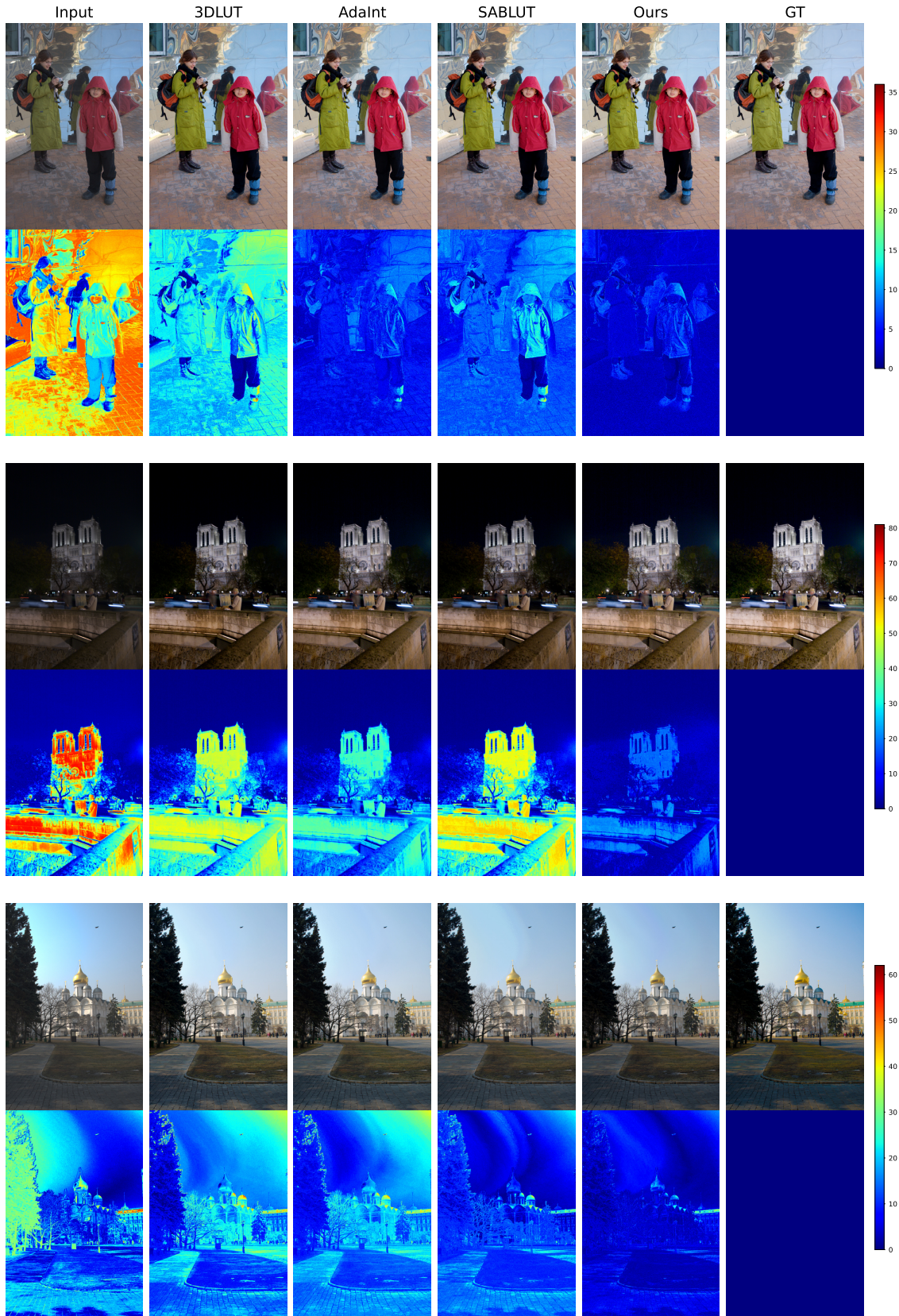


Figure 9. Qualitative comparisons for photo retouch task on the FiveK dataset [3]. The error maps at the bottom of each picture present differences with ground truth. Each color on error map indicates the degree of error based on the corresponding color bars on the right.



Figure 10. Qualitative comparisons for photo retouch task on the PPR10K dataset [28]. The error maps at the bottom of each picture present differences with ground truth. Each color on error map indicates the degree of error based on the corresponding color bars on the right.

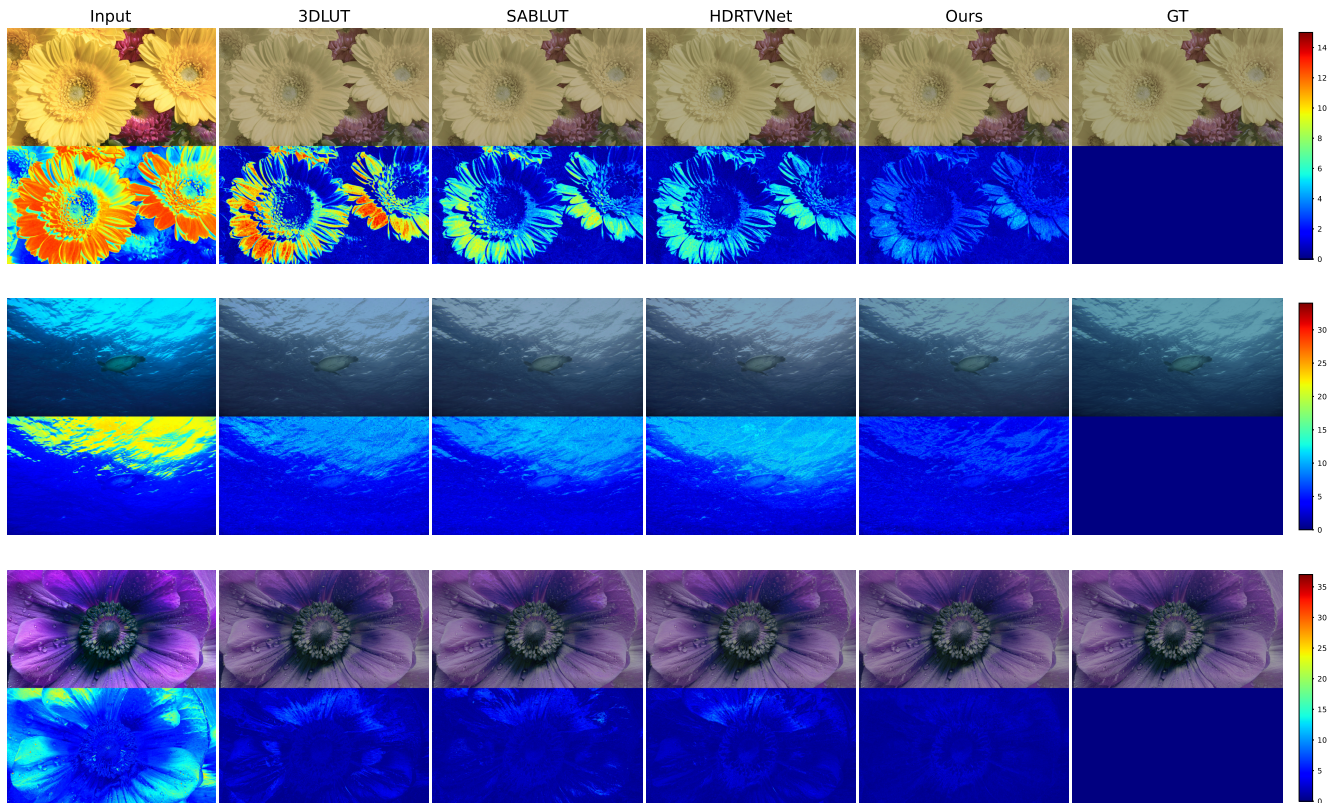


Figure 11. Qualitative comparisons for SDRTV-to-HDRTV task on the HDRTV1K dataset [54]. The error maps at the bottom of each picture present differences with ground truth. Each color on error map indicates the degree of error based on the corresponding color bars on the right.